

PROTECTION AND IDENTIFICATION OF THERMOACOUSTIC AZIMUTHAL MODES

G. Ghirardo*, F. Gant, F. Boudy, M. R. Bothien

Ansaldo Energia Switzerland
 Haselstrasse 18, Baden 5401, Switzerland

ABSTRACT

This paper first characterizes the acoustic field of two annular combustors by means of data from acoustic pressure sensors. In particular the amplitude, orientation, and nature of the acoustic field of azimuthal order n is characterized. The dependence of the pulsation amplitude on the azimuthal location in the chamber is discussed, and a protection scheme making use of just one sensor is proposed. The governing equations are then introduced, and a low-order model of the instabilities is discussed. The model accounts for the nonlinear response of M distinct flames, for system acoustic losses by means of an acoustic damping coefficient α and for the turbulent combustion noise, modelled by means of the background noise coefficient σ . Keeping the response of the flames arbitrary and in principle different from flame to flame, we show that, together with α and σ , only the sum of their responses and their $2n$ Fourier component in the azimuthal direction affect the dynamics of the azimuthal instability. The existing result that only this $2n$ Fourier component affects the stability of standing limit-cycle solutions is recovered. It is found that this result applies also to the case of a non-homogeneous flame response in the annulus, and to flame responses that respond to the azimuthal acoustic velocity. Finally, a parametric flame model is proposed, depending on a linear driving gain β and a nonlinear saturation constant κ . The model is first mapped from continuous time to discrete time, and then recast as a probabilistic Markovian model. The identification of the parameters $\{\alpha, \beta, \kappa, \sigma\}$ is then carried out on engine timeseries data. The optimal four parameters $\{\alpha, \sigma, \beta, \kappa\}$ are estimated as the values that maximize the data likelihood. Once the parameters have been estimated, the phase space of the identified low-order problem is discussed on

selected invariant manifolds of the dynamical system.

NOMENCLATURE

α	equivalent acoustic damping coefficient, see (5)
β	equivalent linear driving coefficient, see (13)
χ	nature angle of the acoustic field, quantifying how much the system is standing vs spinning, see (2) and Fig. 2
Δt	timestep, i.e the reciprocal of the sampling frequency
$\Delta\omega$	filtering bandwidth of the rectangular frequency domain filter centered on ω_0
η_1, η_2	time varying coefficients of a projection on standing modes, see (1)
κ	nonlinear saturation constant, see (13)
μ_z	quaternion-valued, additive white gaussian noise, i.e. $\mu_z = \mu_0 + i\mu_1 + j\mu_2 + k\mu_4$ where each $\mu_r, r = 0, 1, 2, 3$ is real-valued additive white gaussian noise
ω_0	angular frequency of the azimuthal instability
σ	equivalent noise intensity level, see (4)
Θ	set of four parameters describing the system dynamics, introduced after (13)
θ	azimuthal coordinate of the cylindrical coordinate system, spanning $[0, 2\pi]$, see (1)
$\theta^{(2n)}$	phase of the $2n$ -azimuthal component of the flame responses, see (7) and the appendix
θ_0	orientation angle of one of the acoustic pressure antinodes of the acoustic field, see (2) and Fig. 2
φ	slowly varying temporal phase of the thermoacoustic instability, see (2)
A	slowly varying amplitude of the whole acoustic pressure field in the combustion chamber, see (2) and Fig. 2

*contact author: giulio.ghirardo@ansaldoenergia.com

\bar{A}	estimate of the mean amplitude of oscillation $E[A]$
$A_p(\theta)$	slowly varying envelope amplitude of the acoustic pressure in the combustion chamber, as function of the azimuthal location θ , see (3)
c	speed of sound
$E[x]$	Expected value of the variable x , i.e. $E[x] = \int x P(x) dx$
$\mathcal{L}(\Theta \tilde{x}_{2:T})$	Likelihood function of the parameters Θ for one fixed, observed timeseries $x_{2:T} = \tilde{x}_{2:T}$. It measures the goodness of fit of the model, given the observed time-series, as function of Θ , see (18)
M	number of equispaced flames in the annular combustor
m	integer index referring to the m -th flame or burner or segment, from 0 to $M - 1$
n	azimuthal order of the thermoacoustic instability, see (1)
$N^{(0)}$	sum of all the flame responses, see (7) and the appendix
$N^{(2n)}$	absolute value of the $2n$ -azimuthal component of the flame responses, see (7) and the appendix
$P(x), p(x)$	PDF of the variable x
$P(x_t x_{t-1}; \Theta)$	PDF of the variable x_t at instant t , conditional on the value of the variable x_{t-1} at the previous time instant, for a given set of parameters Θ , see (17)
PDF	Probability Density Function
Q_θ	describing function of the flame response and of the acoustic losses, projected on the axial and radial mode shape, introduced in (6). Q_θ describes the contribution over an azimuthal sector of azimuthal width $d\theta$, because it is integrated over the azimuthal coordinate θ in (4)
Q_m	Contribution to Q_θ of the m -th flame. Initially kept generic, then fixed in (13)
$Q_{\theta, \text{flames}}$	Part of Q_θ representing the response of the flames, see (6)
T	number of samples in the timeseries
t	continuous time variable or discrete time index in the section on the maximum likelihood estimate
$x_{1:T}$	set of random samples of the system state x , ordered from time index $t = 1$ to time index $t = T$
$\tilde{x}_{1:T}$	recorded timeseries of $x_{1:T}$, i.e. a specific realization of the samples $x_{1:T}$ of the state x , assumed ergodic

INTRODUCTION

Thermoacoustic pulsations are one of the challenges of combustion applications [1]. They can lead to noise transmission to downstream components, increase of pollutants' emissions, and structural damage of the combustor hardware [2]. The level of acoustic pressure pulsations in gas turbines combustors is of the order of 1-2% of the mean operating pressure [3], and ever increasing operating pressures needed for higher efficiency are pushing pulsation levels higher, of the order of 1 bar. We focus on thermoacoustic pulsations of one common combustor architecture, the annular combustor, specifically on the annular combustors of the Ansaldo Energia GT26 engine [4] as presented in

Fig. 1. The air from the compressor diffuses first in an annular plenum, from which it passes through a set of M burners into the first annular combustion chamber, which is in turn connected to the high pressure (HP) turbine. The air then enters a second annular combustion chamber before entering the second low pressure (LP) turbine. In the development process, the acoustic response of burners and flames is typically first characterized experimentally as single burners at atmospheric conditions, and then the full annular system can be modelled as a network of acoustic elements [5, 6]. Atmospheric tests need to be designed to guarantee the transferability between atmospheric tests and engine conditions, e.g. regarding correct geometrical scalings [7, 8] and reproduction of the correct flame shape [9, 10, 11]. Because of these challenges, it is crucial to correctly identify and characterize pulsation data of annular engines [12].

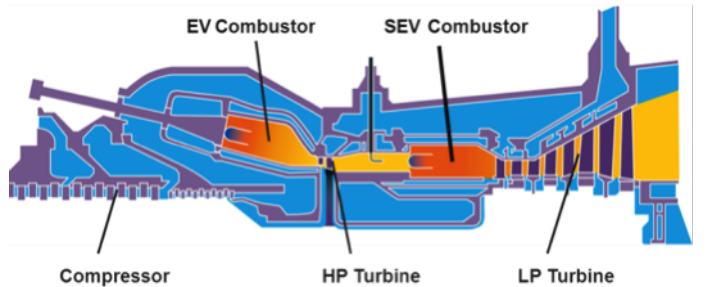


FIGURE 1: Sketch of the longitudinal cut of a GT26 gas turbine. In this paper we present results of pulsation amplitudes of the first annular combustor (EV combustor) and second annular combustor (SEV combustor).

Thermoacoustic modes can develop in the annulus in the azimuthal direction, and are the topic of this paper. We focus in particular on cases where thermoacoustic azimuthal modes occur at one angular frequency ω_0 ¹. Because of the rotational symmetry of the combustor, these modes occur in pairs, where to each pair corresponds an integer azimuthal order n . The two modes in each pair are to a good approximation [13] degenerate, i.e. share the same eigenfrequency, and span a space of dimension two. One can choose with freedom a basis for each space, with the most common choices being two standing waves $\{\cos(n\theta), \sin(n\theta)\}$ and two counter-rotating spinning waves $\{\cos(n\theta - \omega_0 t), \sin(n\theta + \omega_0 t)\}$. One can then project the problem on these bases and either characterize the system dynamics or identify the parameters that define the response of the flames [14, 15, 16, 17, 18, 19]. Alternatively, a model for the flame response is not assumed, and what is identified is the describing function of the flames minus the acoustic losses, projected on the

¹and its multiples $2\omega_0, 3\omega_0, \dots$

azimuthal modes [13]. In all these works the two coefficients $\eta_1(t)$ and $\eta_2(t)$ of the two elements of the basis are identified. For example, when the two standing modes are used as basis, the acoustic pressure field is written as:

$$p(\theta, t) = \eta_1(t) \cos(n\theta) + \eta_2(t) \sin(n\theta) \quad (1)$$

where n is the azimuthal order of the instability and θ is the azimuthal coordinate, periodic in $[0, 2\pi]$. One then derives the governing equations for η_1 and η_2 , which show that they behave as weakly nonlinear oscillators with angular frequency ω_0 , and standing and spinning waves occur as synchronized states of the two oscillators. Equation (1) can be rewritten as [20]:

$$\begin{aligned} p(\theta, t) = & A \cos(n(\theta - \theta_0)) \cos(\chi) \cos(\omega_0 t + \varphi) + \\ & A \sin(n(\theta - \theta_0)) \sin(\chi) \sin(\omega_0 t + \varphi) \end{aligned} \quad (2)$$

where the variables $(A, n\theta_0, \chi, \varphi)$ depend on the time t . The three variables $\{A, n\theta_0, 2\chi\}$ can be interpreted as spherical coordinates, as presented in Fig. 2. The factor A multiplies linearly the whole right hand side of (2) and is then called the slowly varying amplitude of the azimuthal instability. The angle χ is called the nature angle, because it describes the nature of the azimuthal instability, i.e. whether it is standing ($\chi = 0$, on the equator in Fig. 2) or spinning, either anticlockwise ($2\chi = \pi/2$, North pole in Fig. 2), or clockwise ($2\chi = -\pi/2$, South pole in Fig. 2), as discussed in detail in [20]. In particular the angle 2χ is the latitude angle on the sphere of Fig. 2. Finally, the angle θ_0 describes the azimuthal location θ at which the acoustic pulsation is maximum, and is then called the orientation angle. This is the longitude angle in Fig. 2.

This paper discusses how to exploit the new ansatz (2) to characterize the dynamics, design protection schemes and identify the system structure from timeseries of a running engine. For the identification part, we propose to estimate the parameters of the model as the values of the parameters that maximize the likelihood of observing the timeseries. To calculate this, the model of the system is recast as a probabilistic model, and the Markovian property is used to ease the calculation of the likelihood.

ACOUSTIC FIELD CHARACTERIZATION

This section presents the reconstruction of the azimuthal acoustic pressure field of the annular combustor and its characterization. We study the pulsation at a fixed operating condition of one engine based on timeseries data. Pulsation sensors mounted in the SEV combustor of Fig. 1 record timeseries of acoustic pulsations of azimuthal order $n = 3$ with a clear peak at frequency ω_0 . The considered engine has the sensors placed at different,

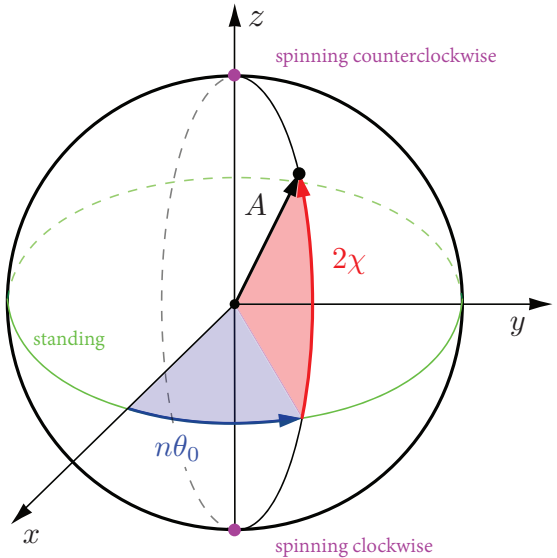


FIGURE 2: Poincaré sphere representation of an azimuthal instability of order n , as presented in (2). The radius A describes the amplitude of acoustic pressure oscillation, the nature angle 2χ describes whether the system is spinning (at the poles) or standing (on the equator) and the angle $n\theta_0$ describes the location of the pressure antinode of the standing component of the instability, as detailed in [20].

not equally spaced, azimuthal locations in the annular combustor. The distance in the axial direction between sensors is acoustically compact in comparison to the wavelength $2\pi c/\omega_0$, where c is the speed of sound in the combustion chamber. The length of the timeseries of the sensors account for a number of limit cycles between 5'000 and 15'000, and are sampled at a frequency such that more than 50 points are sampled for each acoustic period. The timeseries are band-pass filtered in frequency domain with a bandwidth $\Delta\omega/\omega_0 = 0.5$ and then used in the multi-microphone method [21, 22] to reconstruct the coefficients $\eta_1(t)$ and $\eta_2(t)$ appearing in (1). From these two coefficients the four variables $\{A, \chi, n\theta_0, \varphi\}$ are reconstructed as detailed in [20]. The statistics of these quantities are discussed next.

The joint probability density function (PDF) of the amplitude A and of the nature angle χ is presented in Fig. 3. This is estimated as a 2D histogram of the timeseries $\{A(t), \chi(t)\}$ with 17 bins per variable in the observed range, then presented as a contour plot. The color allows to appreciate how often the system stays in a certain state. In particular, the system is rarely in the following states: *i*) at low amplitudes close to zero, because the background noise pushes it away from there; *2*) at amplitudes higher than 1.5, because the flames' gains are lower than the acoustic damping there; *3*) close to the poles at $2\chi = \pm\pi/2$, because the background noise pushes it away from there [23]. Instead, there is a clear peak of the PDF for system states that are between standing and spinning anticlockwise, where the system lingers for most of the time. In this Figure and in the following,

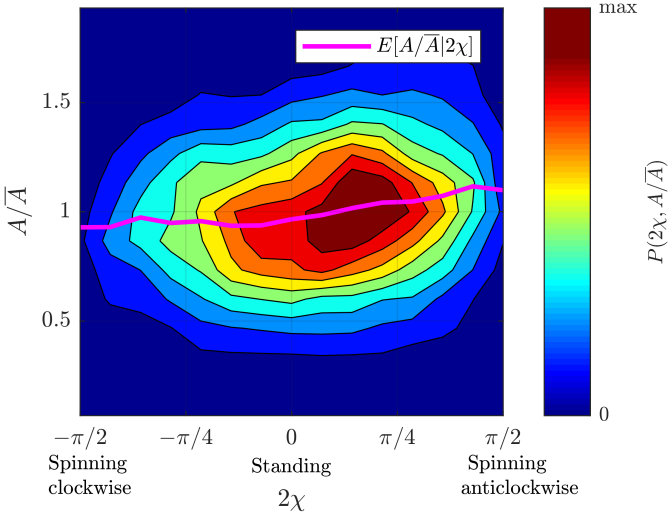


FIGURE 3: Joint statistics of the amplitude A and of the nature angle 2χ in the SEV combustor for an instability of azimuthal order $n = 3$. The system has a clear preference for standing states because the PDF peaks at $2\chi \approx 0$. The dependence of the mean value of amplitude on the nature angle is presented with a magenta line, showing a higher amplitude A when the mode is spinning anticlockwise as compared to when it is standing or spinning clockwise. In this Figure and in the following amplitudes A are nondimensionalized with respect to the mean amplitude \bar{A} , and the colorscale is linear and always between zero and the maximum value.

all amplitudes are nondimensionalized with respect to the mean pulsation amplitude \bar{A} .

The joint PDF of the amplitude A and of the orientation angle $n\theta_0$ is presented in Fig. 4. The dependence on the orientation angle of the PDF is weak. The same applies to the mean amplitude for a given angle $n\theta_0$, presented with a blue line.

One different amplitude to consider is the local acoustic pressure amplitude $A_p(\theta)$ at a certain azimuthal angle θ in the combustion chamber. For example, for the particular case of a purely standing acoustic field, A_p depends on θ because there are clearly defined pressure nodes and antinodes in the combustion chamber. One can calculate the local slowly varying amplitude of acoustic pressure at one location θ as:

$$A_p(\theta) \equiv A \sqrt{\cos^2[n(\theta - \theta_0)] \cos^2(\chi) + \sin^2[n(\theta - \theta_0)] \sin^2(\chi)} \quad (3)$$

which appeared first in [24, Fig. 2b as $R(\theta)$]. One observes from (3) that if the mode is exactly spinning ($2\chi = \pm\pi/2$) one recovers a uniform amplitude $A_p(\theta) = A$ in the whole annulus, while if the mode is exactly standing ($\chi = 0$) the amplitude has structure $A_p(\theta) = A|\cos[n(\theta - \theta_0)]|$ with one pressure antinode

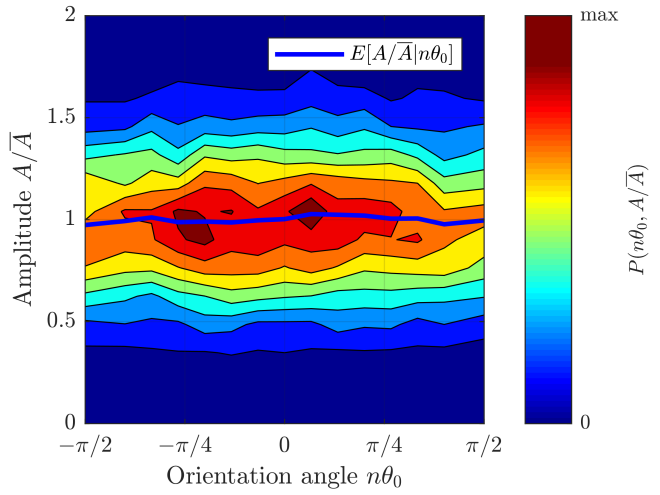


FIGURE 4: Joint probability density function (PDF) of the amplitude A and of the orientation angle $n\theta_0$ of the pressure antinode of the standing component of the mode, for a pulsation mode of azimuthal order $n = 3$ in the SEV combustor. The PDF is quite uniform with respect to the orientation angle $n\theta_0$ close to 0. The blue line represents the mean value of the amplitude A conditioned on the orientation angle $n\theta_0$, confirming the approximate homogeneity.

at the azimuthal angle θ_0 . The PDF of $A_p(\theta)$ as function of θ is presented in Fig. 5. We observe a rather homogeneous pulsation amplitude as function of θ , consistently with Fig. 4, where the amplitude A has no clear preferential orientation angle $n\theta_0$.

PROTECTION

This section discusses how, based on the position of a protection sensor, a protection limit based on its value can be fixed. The previous section discussed in Fig. 5 how the PDF of the local pulsation amplitude depends on the location θ in the annulus. For this case, regarding pulsations in the SEV combustor with azimuthal order $n = 3$, the local amplitude $A_p(\theta)$ is quite constant as function of θ , so that the pulsation sensor θ_p provides a good estimate of the maximum pulsation amplitude regardless of its position θ_p , and an upper limit A_{limit} can be set for protection directly on the probe. Typically this limit corresponds to a certain percentile of acoustic pulsation –say the 98th percentile, which should not be exceeded for a certain time interval and under certain conditions.

Azimuthal pulsations are not however always uniform in the annulus. For example, we present in Figs. 6 and 7 the case of pulsations of azimuthal order $n = 2$ in the EV combustor at a different operating condition, filtered with a bandwidth $\Delta\omega/\omega_0 = 0.35$. In this second case Fig. 6 shows that there is a preferential orientation angle $n\theta_0 = 0$ where the system exhibits a larger amplitude A^2 . When one considers the local am-

²the frame of reference was rotated so that the largest amplitude occurs at Copyright © 2020 by ASME

plitude of pulsation $A_p(\theta)$ in the annulus, as presented in Fig. 7, four characteristic locations where the amplitude is higher, at $\theta = r\pi/2$, $r = 0, 1, 2, 3$ are found. These locations correspond to the $2n = 4$ locations of preferred position of the four pressure antinodes of the azimuthal instability of order $n = 2$. They correspond to the single peak at $n\theta_0 = 0$ of Fig. 6.

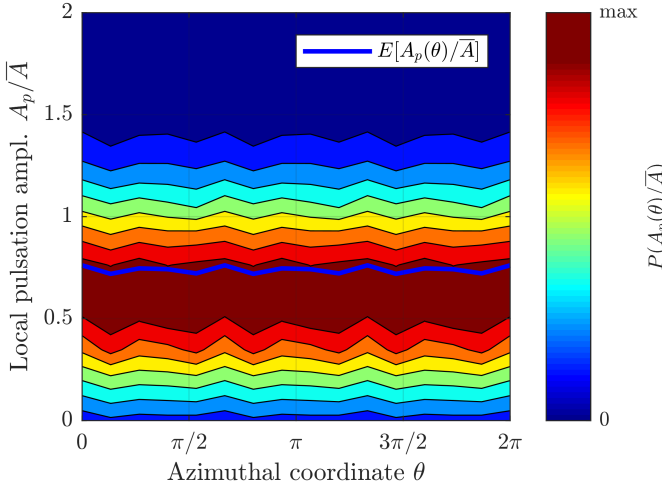


FIGURE 5: Probability density function (PDF) of the local pulsation amplitude $A_p(\theta)$ as function of the azimuthal location θ , for a pulsation mode of azimuthal order $n = 3$ in the SEV combustor. The local amplitude A_p is calculated from the data of Fig. 4 by means of (3). The mean amplitude for a given angle θ is presented with a blue line. The result does not depend on the angle θ to a good approximation.

In this case, the location θ_p of the protection sensor may not match one of the locations $\theta = r\pi/2$, $r = 0, 1, 2, 3$ where the amplitude is largest, and then it may measure a pulsation amplitude that underestimates the maximum amplitude in the annulus. One then first determines the percentile of pulsation at which the maximum amplitude in the annulus, at $\theta = 0$, matches the limit A_{limit} . Once this percentile is found – say the 98th percentile – one recovers the limit on the protection sensor as the amplitude $A_{\text{limit,probe}}$ at which $A_p(\theta_p)$ is at the same percentile.

Up to this point, the system has been described in terms of meaningful physical features but without discussing which underlying physical equations govern the observed dynamics. These equations are discussed next, initially by keeping the flame response generic. In a second step, a simple structure for the flame response is employed to make the model numerically tractable. This allows the identification of the system, which is an important step needed to then assess possible mitigation strategies.

$$\theta = 0.$$

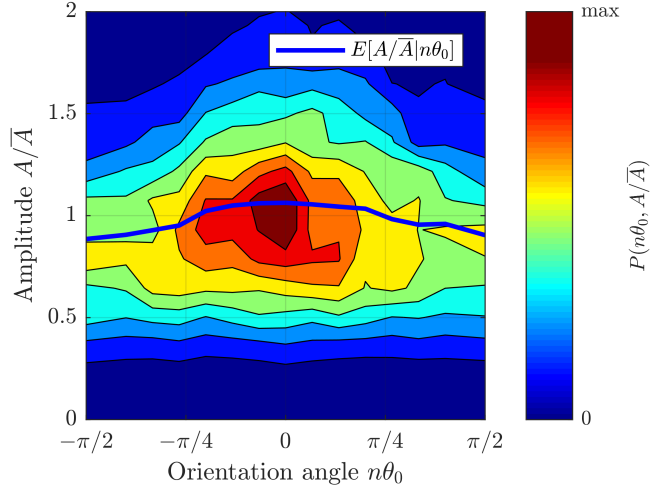


FIGURE 6: Joint probability density function (PDF) of the amplitude A and of the orientation angle $n\theta_0$ of the pressure antinode of the standing component of the mode, for a pulsation mode of azimuthal order $n = 2$ in the EV combustor (the orientation angle $n\theta_0$ was first wrapped between $-\pi/2$ and $\pi/2$). The PDF peaks at a preferential orientation angle $n\theta_0$ close to 0. The blue line represents the mean value of the amplitude A conditioned on the orientation angle $n\theta_0$.

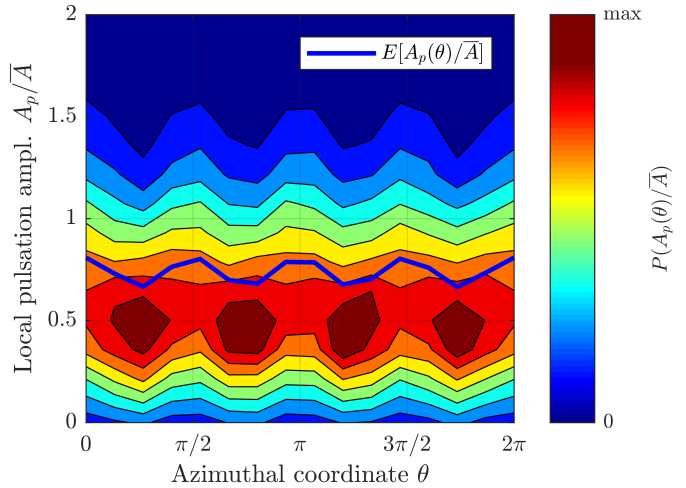


FIGURE 7: Probability density function (PDF) of the local pulsation amplitude $A_p(\theta)$ as function of the azimuthal location θ , for a pulsation mode of azimuthal order $n = 2$ in the EV combustor. The local amplitude A_p is calculated from the data of Fig. 6 by means of (3). The peak of preferred location of $n\theta_0$ in Fig. 6 maps here to $2n = 4$ locations, since the azimuthal order is $n = 2$. These locations are multiples of $2\pi/2n = \pi/2$, where the tails of the PDFs are longer in the vertical direction and the mean amplitudes, presented with a blue line, are also higher.

THE MODEL

This section derives a set of ordinary differential equations of the four variables $A, n\theta_0, \chi, \varphi$ that have been characterized. The dynamics of the system are discussed in general terms, and a brief discussion of the fixed points of the system is presented.

The equations are obtained by substituting the ansatz (2) into the fluctuating mass and momentum conservation equations in cylindrical coordinates, and considering their variation in the azimuthal direction [23]:

$$\begin{aligned} (\ln A)' + (n\theta'_0 + \varphi' \sin(2\chi))i + \varphi' \cos(2\chi)j - \chi'k = \\ + \frac{1}{2} \frac{1}{2\pi} \int_0^{2\pi} \left(e^{i2n(\theta-\theta_0)} e^{k\chi} + e^{-k\chi} \right) Q_\theta d\theta e^{k\chi} \\ + \left(-\frac{\omega}{2} + \frac{\omega_0^2}{2\omega} \right) e^{-k\chi} j e^{k\chi} + \frac{\sigma^2}{4A^2} (1 + \tan(2\chi)k) + \frac{\sigma}{\sqrt{2A}} \mu_z \end{aligned} \quad (4)$$

where i, j, k are the three imaginary units of quaternion algebra [25], the stochastic differential equation (4) has to be interpreted in the Itô sense, and the prime denotes a derivative with respect to the time variable t . The model (4) and its derivation can be found in [23], and only a brief summary is presented next. The left hand side of (4) describes the evolution of the four variables of interest $\{A, n\theta_0, \chi, \varphi\}$ as a function of time. The right hand side of (4) describes the vector field that the four variables follow. In particular the second line in (4) is the contribution over the annulus of Q_θ , which is the projection of the describing functions of the flames and of the acoustic losses on the azimuthal mode [13]:

$$Q_\theta = 2\pi Q_{\theta, \text{flames}}(A, \chi, n\theta_0) - M\alpha \quad (5)$$

where the last term describes the acoustic damping of the system, assumed linear, by means of the coefficient α , and $M = 24$ is the number of burners of the combustor³. For a linearly unstable combustor, the real part of the whole second line is positive at small amplitudes A , so that it pushes the system state away from the origin. For a supercritical case, this real part then decreases monotonically as function of amplitude (because the flames saturate nonlinearly) and becomes negative, keeping the system state always at finite amplitudes A .

The first term on the third line of (4) describes how the frequency of oscillation ω may vary from ω_0 , depending on the angle χ which appears in the two exponentials. This can lead to small changes of the oscillation frequency, depending on whether the mode is standing with $\chi = 0$ or spinning with $2\chi = \pm\pi/2$.

Ending the analysis of (4), the last two terms on the third line of (4) depend on the intensity σ of the background noise. These terms arise because of the random HRR fluctuations of the

turbulent flame [26, 27] and are modelled here as stochastic [28], with μ_z being a quaternion-valued additive white gaussian noise process.

We allow the flames to respond generically to the acoustic field, which is fully described by the three variables $\{A, \chi, n\theta_0\}$. In particular both effects of the acoustic pressure and of the azimuthal acoustic velocity on the heat release rate response are captured [29, 17, 30, 31, 32, 33]. Exploiting the fact that each flame is acoustically compact, we can rewrite $Q_{\theta, \text{flames}}$ as:

$$Q_{\theta, \text{flames}} = \sum_{m=0}^{M-1} Q_m(A, \chi, n(\theta_0 - \theta_m)) \delta(\theta - \theta_m) \quad (6)$$

where $\delta(x)$ is the Dirac distribution, and θ_m is the location of the m -th burner, $\theta_m = 2\pi m/M$, $m = 0, 1, \dots, M-1$, and the projected flame describing functions $Q_m = Q_{m,r} + jQ_{m,j}$ may be different from one another, and are assumed here to be real-valued for simplicity, as in many other studies [14, 16, 13]. Under these assumptions the thermoacoustic oscillation frequency ω matches the natural oscillation frequency ω_0 and the first term in the last row of (4) cancels out [34]. As discussed in the appendix, with the choices (5,6) the model (4) simplifies to:

$$\begin{aligned} (\ln A)' + (n\theta'_0 + \varphi' \sin(2\chi))i + \varphi' \cos(2\chi)j - \chi'k = \\ \frac{1}{2} \left[\frac{1}{2} N^{(2n)} e^{i2n\theta^{(2n)}} e^{2k\chi} + N^{(0)} - M\alpha \right] + \frac{\sigma^2}{4A^2} (1 + \tan(2\chi)k) + \frac{\sigma}{\sqrt{2A}} \mu_z \end{aligned} \quad (7)$$

where the coefficients $\{N^{(r)}, r = 0, \dots, M/2\}$ are the Fourier coefficients of the flame responses in the azimuthal direction, which are defined in the appendix in eq. (25). In particular $N^{(0)}$ is the sum of all the flame responses, and $N^{(2n)}$ and $\theta^{(2n)}$ describe the $2n$ azimuthal component of the flame responses and are respectively the non-negative amplitude and the phase of such component. Similarly to the describing function Q_m introduced in (6), also these Fourier coefficients depend on the variables $\{A, \chi, n\theta_0\}$. Equation (7) shows that the dynamics of the system, which in (4) depend on M distinct describing functions, are actually driven only by the two functions $N^{(0)}$ and $N^{(2n)} e^{i2n\theta^{(2n)}}$, simplifying the problem.

It is then of interest to study the fixed points of the system (7) when the stochastic noise source μ_z is set to zero. The real part of (7) after some manipulation becomes:

$$A' = \frac{A}{2} N^{(0)} + \frac{A}{4} N^{(2n)} \cos(2n\theta^{(2n)}) \cos(2\chi) + \frac{\sigma^2}{4A} - \frac{M}{2} \alpha A \quad (8)$$

The amplitude A_{lc} at which the right hand side of (8) is zero is

³the damping leads to a linear growth rate of $-M\alpha/2$ in absence of the flame.

the solution of:

$$\begin{aligned} \frac{1}{4}N^{(2n)}(A_{lc}, \chi, n\theta_0) \cos(2n\theta^{(2n)}(A_{lc}, \chi, n\theta_0)) \cos(2\chi) + \\ \frac{1}{2}N^{(0)}(A_{lc}, \chi, n\theta_0) + \frac{\sigma^2}{4A_{lc}^2} = \frac{M}{2}\alpha \end{aligned} \quad (9)$$

where in (9) we explicitly write the dependence of $N^{(0)}$ on its arguments, and a direct dependence of the amplitude A_{lc} on the nature angle 2χ is observed in the term $\cos(2\chi)$. A similar dependence of the mean amplitude of pulsation A on the nature angle 2χ is observed in the engine data of Fig. 3. Equation (9) can be interpreted as an acoustic energy balance, where the left hand side are energy sources and the right hand side are energy sinks, and the amplitude A_{lc} is such that the Rayleigh criterion is zero [24]. Similarly, the k -imaginary part of (7) is, after being multiplied by -1 :

$$\begin{aligned} \chi' &= -\frac{1}{4}N^{(2n)} \cos(2n\theta^{(2n)}) \sin(2\chi) - \frac{\sigma^2}{4A^2} \tan(2\chi) \quad (10) \\ &= -\frac{\sin(2\chi)}{4} \left[N^{(2n)} \cos(2n\theta^{(2n)}) + \frac{\sigma^2}{A^2} \frac{1}{\cos(2\chi)} \right] \end{aligned}$$

Equation (10) shows that only the $2n$ Fourier component $N^{(2n)}$, and not the sum $N^{(0)}$ of the flame responses, affects the nature angle. From (10) one can characterize with generality the nature angles that are fixed points in the χ direction, by looking for solutions for which $\chi' = 0$:

$$N^{(2n)} \cos(2n\theta^{(2n)}) \sin(2\chi) + \frac{\sigma^2}{A^2} \tan(2\chi) = 0 \quad (11)$$

One observes that standing states ($\chi = 0$) are always a solution of (11), regardless of the values of the amplitude A , of the orientation angle $n\theta_0$ and of the flame response. This makes the horizontal plane passing through the equator an invariant manifold, because the vector field in the direction normal to the plane is everywhere zero on it.

Moreover, if $N^{(2n)} \cos(2n\theta^{(2n)})$ is negative, one observes from (11) there may be two additional solutions, at nature angles χ between zero and $\pm\pi/4$. These would be mixed⁴ solutions between the equator and the poles.

One can also look for orientation angles that are zeros of the respective vector field, by looking for states such that $n\theta'_0 = 0$. The location of these zeros can also be drawn from symmetry arguments [24] and is not repeated here. We also note that the vector field in this direction is typically weaker, as will be exemplified from the engine data later.

STANDING STATES IN THE DETERMINISTIC CASE

In the case that the background noise contribution is negligible, as is typical of laminar experiments [35], one can set $\sigma = 0$ in (10):

$$\chi' = -\frac{1}{4}N^{(2n)} \cos(2n\theta^{(2n)}) \sin(2\chi) \quad (12)$$

it is straightforward from (12) to calculate that the stability of standing limit-cycles at $\chi = 0$ depends only on the sign of $N^{(2n)} \cos(2n\theta^{(2n)})$. In particular one recovers the N_{2n} criterion, which states that the standing solutions (when they exist) are stable attractors if $N^{(2n)}(A_{lc}, 0, n\theta_0) \cos(2n\theta^{(2n)})$ is positive [24], where A_{lc} is the amplitude of these solutions⁵. This stability criterion of standing solutions is however obtained here without assuming that the configuration is rotationally symmetric and without assuming that the flames are not affected by the azimuthal velocity, generalizing the theory of [24].

This analysis suggests that it is not necessary to fix a certain flame response structure to derive general criteria on the type of solutions (standing, spinning, mixed) that a certain combustor exhibits and that it is possible to describe the system dynamics in terms of the sum of the flame responses $N^{(0)}$ and their $2n$ azimuthal component $N^{(2n)} e^{i2n\theta^{(2n)}}$. These components in fact affect the stability of spinning and standing solutions, as shown in experiments and in theory [36, 24].

MAXIMUM LIKELIHOOD ESTIMATE

In this section we perform the data assimilation to find the optimal parameters that characterize the pulsation of azimuthal order $n = 3$ in the SEV combustor presented earlier. We leave the identification of the functions $N^{(0)}$ and $N^{(2n)} e^{i2n\theta^{(2n)}}$ for a later study, and prefer instead to reframe the problem as parametric. In particular, focusing now on a single flame, we choose a simple saturating model with monotonous response that depend on the acoustic pressure in the combustion chamber A_p only. This captures the effect that the local pulsation amplitude $A_p(\theta)$ at one burner location modulates the acoustic velocity in the burner by means of the whole system upstream admittance [24], ultimately leading to the response of the flame $Q_{\theta, \text{flames}}$. By assuming a dependence on A_p only, we neglect the effect that the azimuthal velocity may have on the heat release rate response [17, 30, 31, 32, 33].

We constrain the projected describing function Q_m of the m th flame to be real-valued as earlier mentioned and such that in

⁴mixed in the sense of partially spinning and partially standing at the same time.

⁵In the reference [24] the factor $\cos(2n\theta^{(2n)})$ did not appear because it did not play a role in the rotationally symmetric configuration studied there. This applies also later in this paper, where $2n\theta^{(2n)}$ is found to match exactly π on the vertical plane containing the solutions.

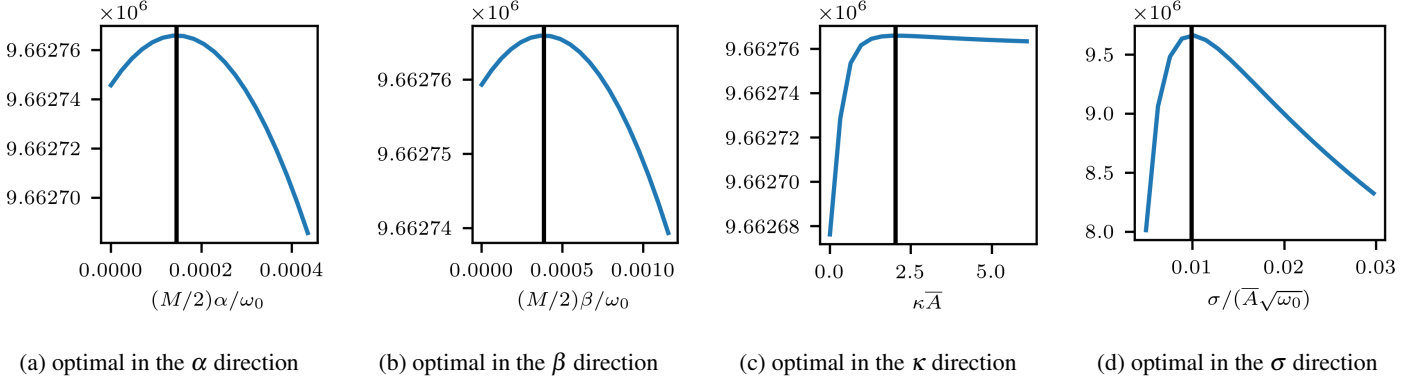


FIGURE 8: Optimality of the identified parameters. In each frame the blue line is the likelihood of observing the engine pulsation data of the SEV combustor of azimuthal order $n = 3$. In each frame, the optimal value of one of the parameters is presented with a vertical black line. In each frame only the parameter presented on the horizontal axis is varied, while keeping the others constant. In all four directions the identified value corresponds to the maximum of the likelihood.

the linear regime it is equal to β at zero amplitude A_p and in the nonlinear regime it tends to 0 in the limit $A_p \rightarrow \infty$:

$$Q_m(A_p) = \beta \frac{2}{\sqrt{\kappa^2 A_p^2 + 1} + 1} \quad (13)$$

which is the describing function of the arctangent function model in time domain $\beta \arctan(\kappa p(t))/\kappa$, with κ a nonlinear saturation constant. The flames lead to a linear growth rate of $M\beta/2$ in absence of noise, i.e. when $\sigma = 0$. This means that in the linear regime and in absence of noise the overall linear growth rate accounting for the damping is $M(\beta - \alpha)/2$. With the choice (13), the model (7) is fully defined by the parameters $\Theta = \{\alpha, \beta, \sigma, \kappa\}$ and we can now tackle the problem of identifying which values of the parameters Θ best describe the measurement data. A discussion of the effect of the parameters on the phase space of the model will come afterwards.

Since the engine data is uniformly sampled, the next step consists of mapping the continuous time differential equation (7) to its discrete counterpart, which maps the state at the timestep t to the state at the timestep $t+1$, by using the Euler-Maruyama scheme [37]:

$$\begin{aligned} (\ln A)_{t+1} + (n\theta_{0,t+1} + \varphi_{t+1} \sin(2\chi_t))i + \varphi_{t+1} \cos(2\chi_t)j - \chi_{t+1}k = \\ (\ln A)_t + (n\theta_{0,t} + \varphi_t \sin(2\chi_t))i + \varphi_t \cos(2\chi_t)j - \chi_t k + \\ \left\{ \frac{1}{2} \left[\frac{1}{2} N^{(2n)}(A_t, \chi_t, n\theta_{0,t}) e^{i2n\theta_t^{(2n)}} e^{2k\chi_t} + N^{(0)}(A_t, \chi_t, n\theta_{0,t}) - M\alpha \right] \right. \\ \left. + \frac{\sigma^2}{4A_t^2} (1 + \tan(2\chi_t)k) \right\} \Delta t + \frac{\sigma}{\sqrt{2}A_t} \sqrt{\Delta t} \mathcal{N}[\mathbf{0}, \mathbf{1}] \end{aligned} \quad (14)$$

where t denotes here a timestep and varies incrementally from an initial condition at $t = 0$ to the total number of samples $t = T$,

and \mathcal{N} is the normal distribution with mean $\mathbf{0} = (0, 0, 0, 0)$ and variance the 4×4 unity matrix $\mathbf{1}$.

We introduce the $4 \times T$ vector x , whose t -th entry is $x_t = (\ln(A_t), n\theta_{0,t}, \varphi_t, \chi_t)$, and a total of T samples are recorded over a time of $T\Delta t$, where Δt is the timestep. One can re-write (14) in terms of x as:

$$\mathbf{C}_t(x_{t+1} - x_t) = f(x_t)\Delta t + \frac{\sigma}{\sqrt{2}A_t} \sqrt{\Delta t} \mathcal{N}[\mathbf{0}, \mathbf{1}] \quad (15)$$

where \mathbf{C}_t is an invertible square matrix depending on x at timestep t and f is defined as the term within curly brackets in (14). One recorded timeseries is one realization of the stochastic system of equations (15), which can be interpreted as a probabilistic model for the variable on the left hand side:

$$\mathbf{C}_t(x_{t+1} - x_t) \propto \mathcal{N} \left[f(x_t)\Delta t, \frac{\sigma^2}{2A_t^2} \Delta t \mathbf{1} \right] \quad (16)$$

In particular, given the process x_t at timestep t , the probabilistic model (16) describes how to draw the sample x_{t+1} given the sample x_t from the normal distribution \mathcal{N} , having fixed all parameters Θ describing the model. This is equivalent to one step of time integration of the stochastic differential equation (14). However, the probabilistic model (16) can also be exploited in a new, different way: given both samples at timestep x_t and at time x_{t+1} , which are assumed to be available from a simulation or engine measurement, it allows the calculation of the probability of the occurrence of the known value x_{t+1} , given the known x_t , again for a fixed set of parameters $\Theta = \{\alpha, \beta, \sigma, \kappa\}$.

Usually one, instead of considering the probability of just one timestep given the previous, considers the probability of the whole recorded timeseries $p(x_{1:T}; \Theta)$, where $x_{1:T}$ denotes the $4 \times T$ vector $\{x_1, x_2, \dots, x_T\}$. Because (14) is Markovian, this can be

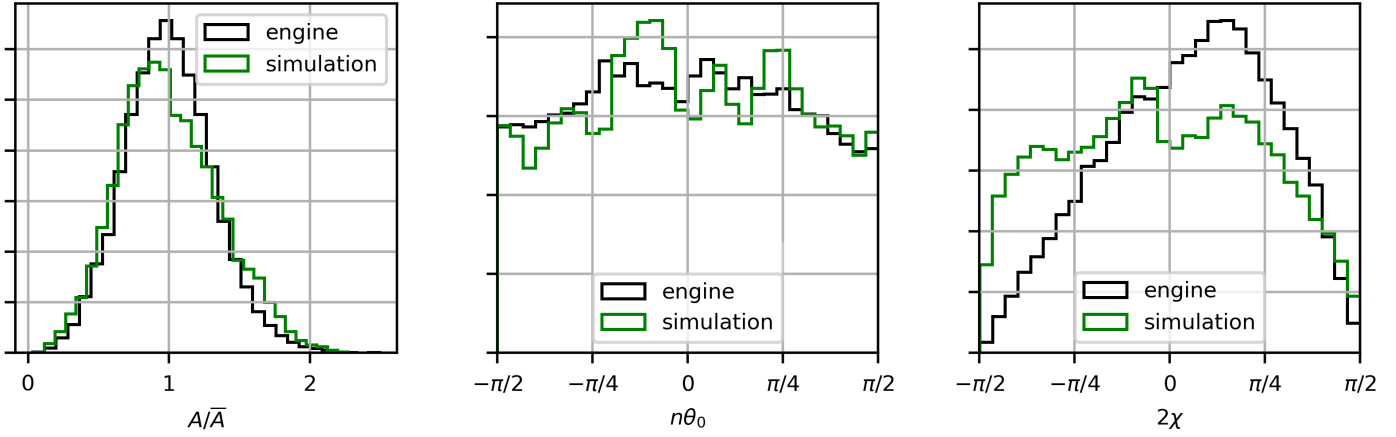


FIGURE 9: Comparison of the statistics of the engine data and of the tuned model, in terms of amplitude A (left), orientation angle $n\theta_0$ of the acoustic field (middle) and nature . The three frames present the probability density functions of the spherical coordinates of the system state on the Poincaré sphere of Fig. 2. . The vertical axis is linear, with the lower limit set to zero, in all three frames

recovered as a product of the probabilities of one timestep at a time as just described:

$$p(x_{2:T}; \Theta) = \prod_{t=2}^T p(x_t | x_{t-1}; \Theta) \quad (17)$$

where the terms on the right hand side can be calculated by means of (16). It is then apparent that the probability p is affected by the choice of the parameters Θ . One then can study this by introducing the likelihood function as:

$$\mathcal{L}(\Theta | \tilde{x}_{2:T}) = p(x_{2:T} = \tilde{x}_{2:T}; \Theta) \quad (18)$$

where $\tilde{x}_{2:T}$ is the measured timeseries. One can then search for the set of parameters Θ that maximises the likelihood (18), carrying out a so-called maximum-likelihood estimate of the parameters Θ .

This method was first validated on data of numerical simulations of (7), showing convergence of the estimated Θ to the values used in the simulations. Then it was applied on the engine data of the SEV annular combustor. The identified optimal values of Θ are presented in Fig. 8 with vertical black lines. In each of the frames, only one of the parameters is varied to check that the identified value is indeed a maximum of the likelihood probability.

PHASE SPACE CHARACTERIZATION

The identified values $\{\alpha, \sigma, \beta, \kappa\}$ fully define the equations (7). We present in Fig. 9 a comparison of the statistics of the engine data and of a stochastic simulation of (7) with the optimal parameters Θ , run with the Euler-Maruyama numerical scheme

with the same nondimensional timestep of the engine and for a duration corresponding to the same number of limit-cycles. We have a good agreement between them in terms of amplitude A (first frame) and of orientation angle $n\theta_0$ (second frame). The third frame shows quite similar results, but a more clear peak in the engine data. The mismatch may be caused by finite time effects, i.e. the fact that the PDFs have not yet converged to their stationary distribution.

We can study the flow of the three variables $\{A, n\theta_0, \chi\}$ on the phase space of Fig. 2. This phase space has three dimensions and is then hard to visualize. We decide to consider some plane cuts of the phase space, and represent the in-plane components of the 3-d flow. Of the many possible planes, we choose to consider two planes that are also invariant manifolds of the system, i.e. such that the normal component of the field to the plane is zero: the vertical plane passing through both poles with longitude angle $n\theta_0 = 0$ and the plane containing the equator line of Fig. 2. We describe the two separately in the next two paragraphs.

In Fig. 10 we discuss the vertical plane cut. In particular we present just half of the results, because of the symmetry of the system. In the top row of the figure we present the sum of the flame responses $N^{(0)}$ and the $2n$ azimuthal component $N^{(2n)}$ and the phase $2n\theta^{(2n)}$ which appear in (7). The radial component of the vector field, i.e. the right hand side of (8), is presented on the second row of Fig. 10 on the left. The colorscale is presented just below the frame, and the colormap is chosen symmetric with respect to the value of zero, where it is white. The locus of this zero is presented also with a black contour. From this frame we conclude that points starting from the origin or at infinity move towards the black contour. The component of the vector field in the direction χ can be calculated as the right hand side of (10). One observes from the top row of Fig. 10 that the product $N^{(2n)}(A, \chi, n\theta_0) \cos(2n\theta^{(2n)})$ appearing on the right

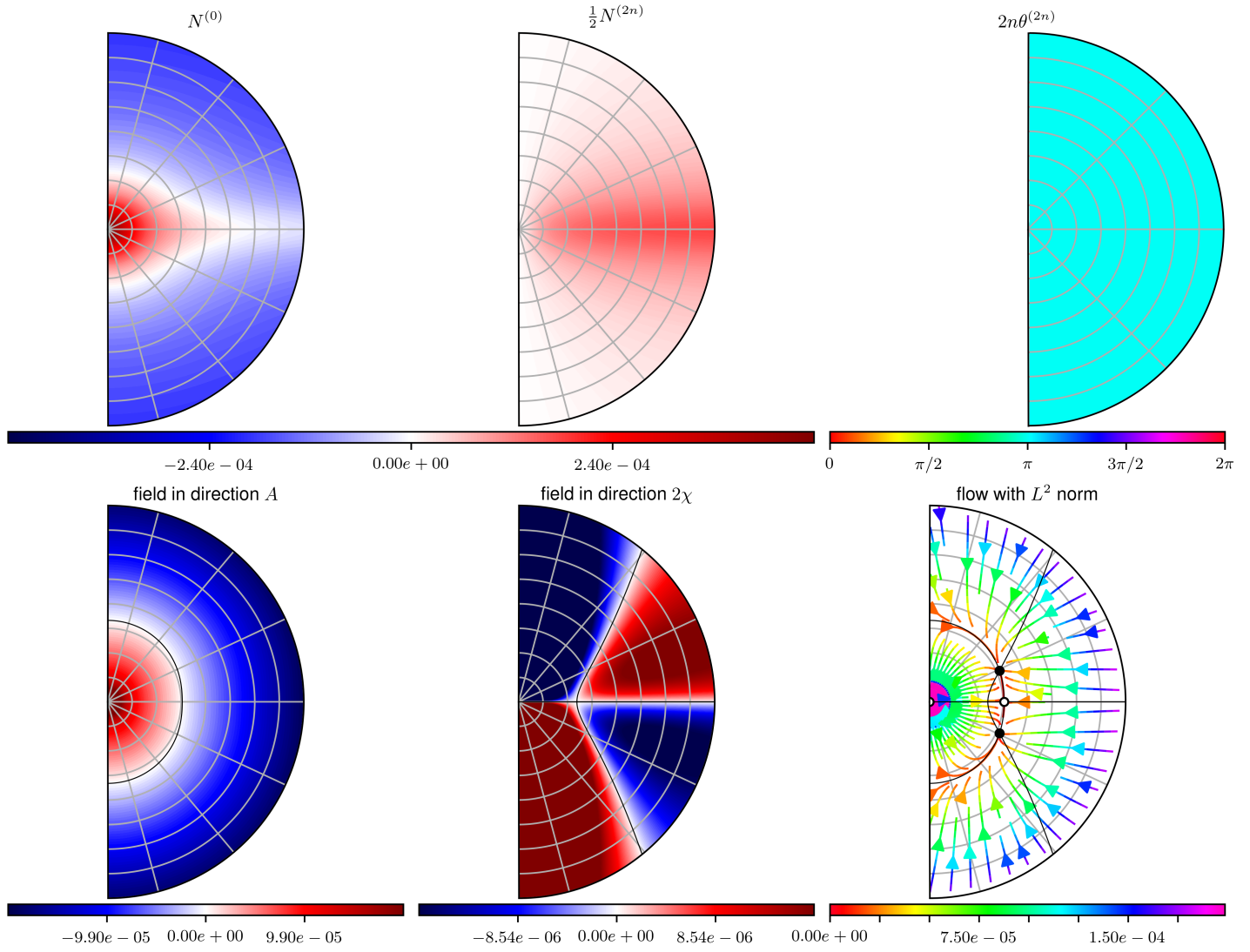


FIGURE 10: vertical cut through the poles of the Poincaré sphere of Fig. 2. The key functions governing the dynamics are presented in the top three frames and the resulting flow fields in the radial and azimuthal direction are presented in the bottom frames, left and middle. Black contour lines are the zeros of the fields. The bottom right plot combines the two flow fields in streamlines. In this last frame fixed points are reported with round markers, filled if they are attractors in the plane and empty if they are repellors or saddles in the plane. The radial coordinate is A/\bar{A} and covers a range from 0 to 2 as in the other Figs. of the paper.

hand side of (10) is negative, so that the first term in (10) pushes the solution to the poles. The second term, proportional to the noise σ^2 , pushes instead the system away from the poles [23] and it is larger at small amplitudes. The total effect is the sum of these two counteracting terms and is presented in the middle of the second row of Fig. 10. In the vicinity of the equator the system state is pushed towards the equator at low amplitudes and towards the poles at large amplitudes. The color of the frame can be interpreted here qualitatively as follows: blue pushes the state south and red pushes the state north. The location of where $\chi' = 0$ is presented also in this frame with black contour lines. The intersections of the contour lines of the first two frames in the second row of Fig. 10 describe the fixed points in this vertical plane. These are presented in the last frame of Fig. 10 with two circles. The filled circles are attractors in the plane, while

empty circles are repellors or saddles. In the same frame also the streamlines of the in-plane flow is presented, colored by its magnitude. As a summary, Fig. 10 shows that the standing solution on the equator is a repellor and that two mixed states close to the equator are attractors in this vertical plane. There are no corresponding peaks in the PDF of the nature angle in Fig. 9. This is attributed to the noise and to how close the three fixed points are.

We analyze next the horizontal equatorial cut, presented in Fig. 11. To this figure the same interpretation of Fig. 10 applies, in terms of colors, black contour lines marking the loci of the zeros and circles marking the fixed points. We observe that the phase $2n\theta^{(2n)}$ is very close to π but not exactly matching π on this plane. This means that $\sin(2n\theta^{(2n)})$ is not exactly zero, and then the term $\frac{1}{4}N^{(2n)}(A, \chi = 0, n\theta_0)\sin(2n\theta^{(2n)})$ that appears in the i -imaginary component of (7) drives the system in

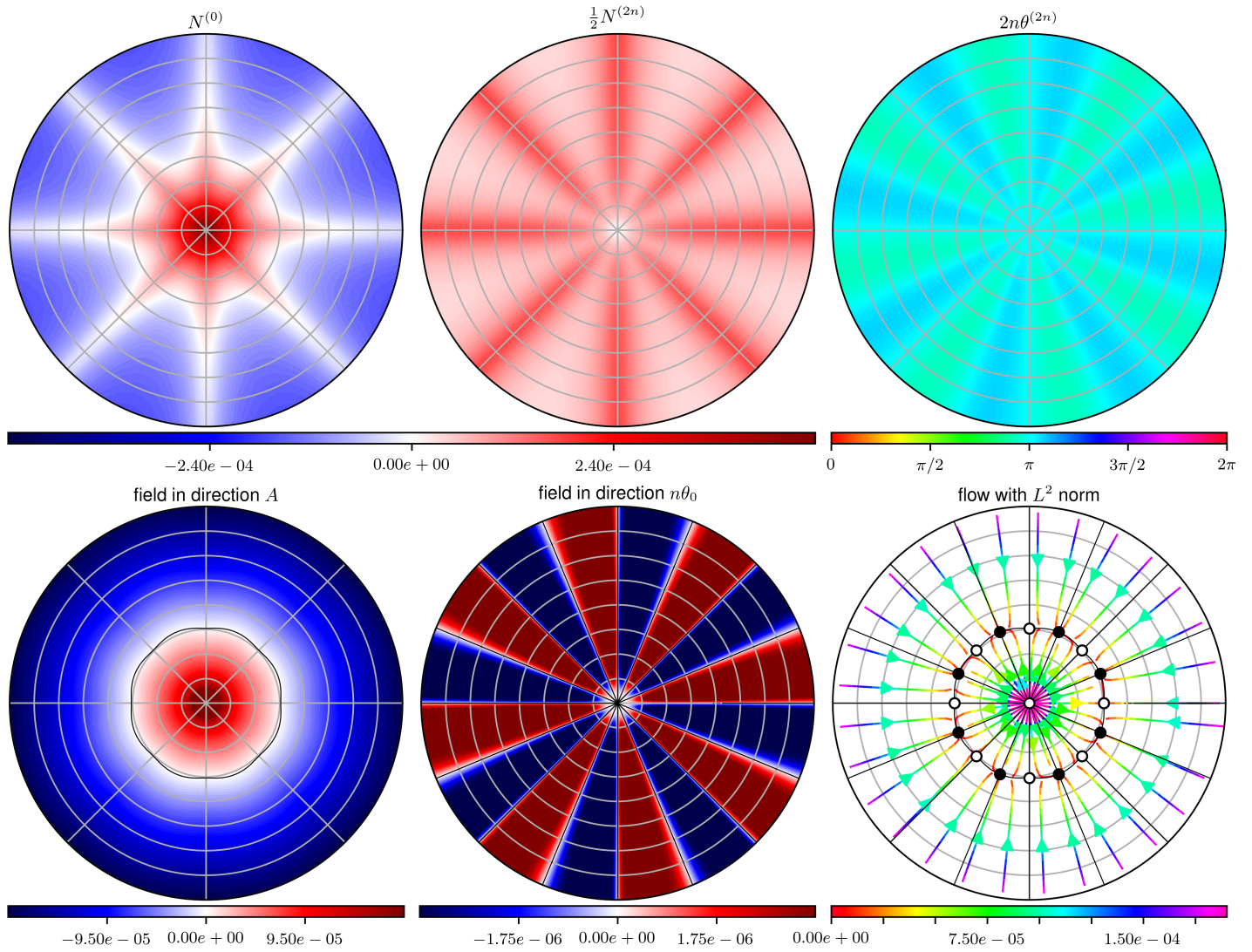


FIGURE 11: Horizontal cut through the equator of the Poincaré sphere. Same information of Fig. 10 applies.

the $n\theta$ direction. This translates in alternating signs of the azimuthal field in the middle frame of the second row of Fig. 11. The color of the frame can be interpreted here qualitatively as follows: blue pushes the state clockwise in the horizontal plane and red pushes the state anticlockwise. Notice however that the magnitude of the color scale in this frame is much smaller than the color scale describing the field in the radial direction (bottom left frame of the same Figure). This is also apparent when looking at the streamlines in the last frame on the second row of Fig. 11. The slight turn of the streamlines in the azimuthal direction is barely visible only close to the fixed points. In this last frame, the fixed points alternate between attractors and saddles. There are no corresponding peaks in the PDF of the orientation angle $n\theta_0$ in Fig. 9. This is attributed both to the noise and to the weakness of the field in this direction.

We conclude this section with a discussion of the role that the four parameters $\Theta = \{\alpha, \beta, \sigma, \kappa\}$ have on the system dynamics and on the phase space, based on (8) and (10). First of all, the instantaneous growth rate of the system goes from $(\beta - \alpha)M/2$

in the linear regime to $-M\alpha/2$ at very large amplitudes. These two numbers determine how fast can the amplitude vary in one limit-cycle, with small values leading to slow variations⁶. Small values of the nonlinear saturation constant κ lead to larger amplitudes because κ describes how gentle is the saturation of the flames as function of amplitude, with small values of κ leading to a flame that saturates only at very large amplitudes. In Figs. 10 and 11, larger amplitudes for the system mean that the fixed points are pushed away from the origin. Based on numerical evidence, a change of the amplitude does not affect the topology of the phase space on the horizontal of Fig. 11. Regarding instead the topology of the phase space in the vertical plane of Fig. 10, this depends on the analysis presented after (10). We have observed that, depending on the flame response and on the nondimensional number $\sigma/(\bar{A}\sqrt{\omega_0})$, the three fixed points presented can coalesce to one attractor. Focusing just on the effect of the noise intensity in this vertical plane, we observe that it pushes the

⁶at amplitudes sufficiently large so that the contribution of the noise is small

system away from the poles by means of the term $-\frac{\sigma^2}{4A^2} \tan(2\chi)$ in (10) [23]. The strength of this effect in the neighbourhood of the mean amplitude $\bar{A} = E[A]$ scales like the square of σ/\bar{A} . This depends then indirectly on \bar{A} , which in turn depends on the non-linear response of the flame and is only loosely dependent on the linear behaviour of the system.

CONCLUSIONS

We have presented statistical results using engine measurements characterising one azimuthal instability of azimuthal order n at angular frequency ω_0 . We have characterized the acoustic field in terms of the amplitude of the acoustic pulsation A , of the orientation angle $n\theta_0$ where the pulsation amplitude is maximum and of the nature angle 2χ describing if the acoustic field rotates or stands. A protection scheme making use of just one pulsation sensor to protect against pulsation is discussed. The scheme accounts for the non-homogeneity of the pulsation amplitude in the azimuthal coordinate.

The governing equations are then presented and a theoretical discussion of the fixed points of the system is carried out, recovering existing theories for the stability of spinning and standing solutions in the homogeneous case. In particular, it is shown that, together with the level of acoustic damping α and of the background noise σ , only the sum of the flame responses and their $2n$ azimuthal component affect the dynamics of the acoustic field. An existing theoretical criterion for the stability of standing solutions at low level of noise σ is also proved to apply to annular combustors where the flame response depends also on the azimuthal acoustic velocity and where the response of the flames is different from flame to flame.

A new methodology is proposed to tune the parameters of a thermoacoustic model as the parameters maximizing the likelihood of the data of the model, which is recast as probabilistic. This is explored on a simplified model where all the flames in the combustor are the same, respond to the level of acoustic pressure at the burner, and are characterized by a linear equivalent flame strength β and a nonlinear saturation κ . This methodology is first validated on simulation data and then applied on engine data, allowing the identification of the model parameters. A comparison between a simulation of the identified system and the engine data is presented with good agreement. Finally the phase space of the identified system is characterized on the Poincaré sphere.

REFERENCES

- [1] Keller, J. J., 1995. "Thermoacoustic oscillations in combustion chambers of gas turbines". *AIAA Journal*, **33**(12), pp. 2280–2287.
- [2] Sewell, J. B., Sobleski, P., and Beers, C., 2004. "Application of Continuous Combustion Dynamics Monitoring on Large Industrial Gas Turbines". In Proceedings of ASME TurboExpo 2004, paper no. GT2004-54310, American Society of Mechanical Engineers, pp. 807–815.
- [3] Scarinci, T., 2005. "Combustion Instability and Its Passive Control: Rolls-Royce Aeroderivative Engine Experience". In *Combustion Instabilities in Gas Turbine Engines: Operational Experience, Fundamental Mechanisms, and Modeling*, T. C. Lieuwen and V. Yang, eds. American Institute of Aeronautics and Astronautics, ch. 4, pp. 65–88.
- [4] Gütthe, F., Hellat, J., and Flohr, P., 2009. "The Reheat Concept: The Proven Pathway to Ultralow Emissions and High Efficiency and Flexibility". *Journal of Engineering for Gas Turbines and Power*, **131**(2), p. 021503.
- [5] Paschereit, C. O., Schuermans, B., Polifke, W., and Mattson, O., 2002. "Measurement of Transfer Matrices and Source Terms of Premixed Flames". *Journal of Engineering for Gas Turbines and Power*, **124**(2), p. 239.
- [6] Schuermans, B., Bellucci, V., and Paschereit, C. O., 2003. "Thermoacoustic modeling and control of multi burner combustion systems". *Proceedings of ASME Turbo Expo 2003*, paper no. 2003-GT-38688.
- [7] Fanaca, D., Alemela, P. R., Hirsch, C., and Sattelmayer, T., 2010. "Comparison of the Flow Field of a Swirl Stabilized Premixed Burner in an Annular and a Single Burner Combustion Chamber". *Journal of Engineering for Gas Turbines and Power*, **132**(7), p. 071502.
- [8] Durox, D., Prieur, K., Schuller, T., and Candel, S., 2016. "Different Flame Patterns Linked With Swirling Injector Interactions in an Annular Combustor". *Journal of Engineering for Gas Turbines and Power*, **138**(10), p. 101504.
- [9] O'Connor, J., Worth, N. A., and Dawson, J. R., 2013. "Flame and flow dynamics of a self-excited, standing wave circumferential instability in a model annular gas turbine combustor". *Proceedings of ASME Turbo Expo 2013*, pp. 1–15.
- [10] Rofi, L., Anisimov, V., Chiarioni, A., Ozzano, C., and Daccà, F., 2014. "Bi-Stable Flame Behaviour of Heavy Duty Gas Turbine Burner". In Proceedings of ASME Turbo Expo 2014, paper no. GT2014-25546, American Society of Mechanical Engineers, pp. 1–11.
- [11] Anisimov, V. V., Chiarioni, A., Rofi, L., Ozzano, C., Hermeth, S., Hannebique, G., Staffelbach, G., and Poinsot, T., 2015. "Bi-Stable Flame Behaviour of Heavy Duty Gas Turbine Burner: RANS, LES and Experiment Comparison". In Proceedings of ASME Turbo Expo 2015, paper no. 42536, American Society of Mechanical Engineers, pp. 1–15.
- [12] Singla, G., Noiray, N., and Schuermans, B., 2012. "Combustion dynamics validation of an annular reheat combustor". In Proceedings of ASME Turbo expo 2012, paper no. GT2012-68684, pp. 1–9.
- [13] Ghirardo, G., Boudy, F., and Bothien, M. R., 2018. "Amplitude statistics prediction in thermoacoustics". *Journal of Fluid Mechanics*, **844**, pp. 216–246.

- [14] Schuermans, B., Paschereit, C. O., and Monkewitz, P., 2006. “Non-Linear Combustion Instabilities in Annular Gas-Turbine Combustors”. In 44th AIAA Aerospace Sciences Meeting and Exhibit. Paper no. AIAA-2006-0549, American Institute of Aeronautics and Astronautics, pp. 1–12.
- [15] Noiray, N., Bothien, M. R., and Schuermans, B., 2011. “Investigation of azimuthal staging concepts in annular gas turbines”. *Combustion Theory and Modelling*, **15**(5), pp. 585–606.
- [16] Noiray, N., and Schuermans, B., 2013. “On the dynamic nature of azimuthal thermoacoustic modes in annular gas turbine combustion chambers”. *Proceedings of the Royal Society A: Mathematical, Physical and Engineering Sciences*, **469**(20120535), pp. 1–15.
- [17] Ghirardo, G., and Juniper, M. P., 2013. “Azimuthal instabilities in annular combustors: standing and spinning modes”. *Proceedings of the Royal Society A: Mathematical, Physical and Engineering Sciences*, **469**, jul, pp. 1–16.
- [18] Bothien, M. R., Noiray, N., and Schuermans, B., 2015. “Analysis of Azimuthal Thermo-acoustic Modes in Annular Gas Turbine Combustion Chambers”. *Journal of Engineering for Gas Turbines and Power*, **137**(6), jun, p. 061505.
- [19] Hummel, T., Berger, F., Schuermans, B., and Sattelmayer, T., 2016. “Theory and Modeling of Non-Degenerate Transversal Thermoacoustic Limit Cycle Oscillations”. *Thermoacoustic instabilities in gas turbines and rocket engines: industry meets academia*(June), pp. 1–13.
- [20] Ghirardo, G., and Bothien, M. R., 2018. “Quaternion structure of azimuthal instabilities”. *Physical Review Fluids*, **3**(11), nov, p. 113202.
- [21] Seybert, A. F., and Ross, D. F., 1977. “Experimental determination of acoustic properties using a two-microphone random-excitation technique”. *The Journal of Acoustical Society of America*, **61**(5), pp. 1362–1370.
- [22] Åbom, M., 1992. “A note on the experimental determination of acoustical two-port matrices”. *Journal of sound and vibration*, **155**(1), pp. 185–188.
- [23] Ghirardo, G., and Gant, F., 2019. “Background noise pushes azimuthal instabilities away from spinning states”. *arXiv:1904.00213v1*, pp. 1–4.
- [24] Ghirardo, G., Juniper, M. P., and Moeck, J. P., 2016. “Weakly nonlinear analysis of thermoacoustic instabilities in annular combustors”. *J. Fluid Mech.*, **805**, oct, pp. 52–87.
- [25] Doran, C., and Lasenby, A., 2003. *Geometric Algebra for Physicists*. Cambridge University Press, Cambridge.
- [26] Strahle, W. C., 1972. “Some results in combustion generated noise”. *Journal of Sound and Vibration*, **23**(1), jul, pp. 113–125.
- [27] Rajaram, R., and Lieuwen, T., 2009. “Acoustic radiation from turbulent premixed flames”. *J. Fluid Mech.*, **637**, oct, pp. 357–385.
- [28] Lieuwen, T., 2003. “Statistical characteristics of pressure oscillations in a premixed combustor”. *Journal of Sound and Vibration*, **260**(1), pp. 3–17.
- [29] Hauser, M., Lorenz, M., and Sattelmayer, T., 2011. “Influence of Transversal Acoustic Excitation of the Burner Approach Flow on the Flame Structure”. *Journal of Engineering for Gas Turbines and Power*, **133**(4), p. 041501.
- [30] O’Connor, J., and Acharya, V. S., 2013. “Development of a flame transfer function framework for transversely forced flames”. *Proceedings of ASME Turbo Expo 2013*, paper no. GT2013-95900.
- [31] Acharya, V. S., and Lieuwen, T., 2014. “Response of non-axisymmetric premixed, swirl flames to helical disturbances”. In Proceedings of ASME Turbo Expo 2014, paper no. GT2014-27059, ASME, pp. 1–13.
- [32] Saurabh, A., and Paschereit, C. O., 2017. “Dynamics of premixed swirl flames under the influence of transverse acoustic fluctuations”. *Combustion and Flame*, **182**, pp. 298–312.
- [33] Saurabh, A., and Paschereit, C. O., 2019. “Premixed Flame Dynamics in Response to Two-Dimensional Acoustic Forcing”. *Combustion Science and Technology*, **191**(7), pp. 1184–1200.
- [34] Ghirardo, G., Juniper, M. P., and Bothien, M. R., 2017. “The effect of the flame phase on thermoacoustic instabilities”. *Combustion and Flame*, **187**, pp. 165–184.
- [35] Bourgouin, J.-F., Durox, D., Moeck, J. P., Schuller, T., and Candel, S., 2015. “Characterization and Modeling of a Spinning Thermoacoustic Instability in an Annular Combustor Equipped with Multiple Matrix Injectors”. *J. Eng. Gas Turb. Pow.*, **137**, sep.
- [36] Laera, D., Schuller, T., Prieur, K., Durox, D., Camporeale, S. M., and Candel, S., 2017. “Flame Describing Function analysis of spinning and standing modes in an annular combustor and comparison with experiments”. *Combust. Flame*, **184**, oct, pp. 136–152.
- [37] Kloeden, P. E., and Platen, E., 1995. *Numerical solution of stochastic differential equations*, second ed. Springer.

APPENDIX

This appendix shows how (7) is derived from (4). We manipulate the second line of (4), reported here for convenience:

$$\frac{1}{2} \frac{1}{2\pi} \int_0^{2\pi} \left(e^{i2n(\theta-\theta_0)} e^{k\chi} + e^{-k\chi} \right) Q_\theta(A_p(\theta)) d\theta e^{k\chi} \quad (19)$$

We substitute (6) into (5):

$$Q_\theta(A_p) = 2\pi \sum_{m=0}^{M-1} Q_m(A_p(\theta)) \delta(\theta - \theta_m) - M\alpha \quad (20)$$

We then substitute (20) into (19):

$$\begin{aligned} & \frac{1}{2} \sum_{m=0}^{M-1} \left(e^{i2n(\theta_m - \theta_0)} e^{k\chi} + e^{-k\chi} \right) Q_m(A_p(\theta_m)) e^{k\chi} \\ & - \frac{1}{2} \frac{1}{2\pi} \int_0^{2\pi} \left\{ \left(e^{i2n(\theta - \theta_0)} e^{k\chi} + e^{-k\chi} \right) M\alpha e^{k\chi} \right\} d\theta \end{aligned} \quad (21)$$

Because the describing functions Q_m and α are real-valued, (21) simplifies to:

$$\begin{aligned} & \frac{1}{2} \left[\sum_{m=0}^{M-1} e^{i2n(\theta_m - \theta_0)} Q_m(A_p(\theta_m)) \right] e^{2k\chi} + \frac{1}{2} \sum_{m=0}^{M-1} Q_m(A_p(\theta_m)) \\ & - \frac{1}{2} \frac{1}{2\pi} \int_0^{2\pi} \left(e^{i2n(\theta - \theta_0)} e^{k\chi} + e^{-k\chi} \right) e^{k\chi} d\theta M\alpha \end{aligned} \quad (22)$$

The term on the second line of (22) simplifies:

$$-\frac{1}{2} \frac{1}{2\pi} \int_0^{2\pi} e^{i2n(\theta - \theta_0)} d\theta e^{2k\chi} M\alpha - \frac{1}{2} \frac{1}{2\pi} \int_0^{2\pi} d\theta M\alpha = -\frac{1}{2} M\alpha$$

which substituted into (22) gives

$$\frac{1}{2} \left\{ \left[\sum_{m=0}^{M-1} e^{i2n(\theta_m - \theta_0)} Q_m(A_p(\theta_m)) \right] e^{2k\chi} + \sum_{m=0}^{M-1} Q_m(A_p(\theta_m)) - M\alpha \right\} \quad (23)$$

We then write the scalars Q_m , $m = 0, \dots, M-1$ in terms of their discrete Fourier transform:

$$Q_m(A_p(\theta_m)) = \frac{1}{M} \sum_{r=0}^{M/2} N^{(r)} \cos \left[r(\theta_m - \theta^{(r)} - \theta_0) \right] \quad (24)$$

where the Fourier transform coefficients and phases $\{(N^{(r)}, \theta^{(r)}), r = 0, \dots, M/2\}$ depend on $(A, \chi, n\theta_0)$ and can be calculated as:

$$N^{(r)} \equiv (2 - \delta_{r,0} - \delta_{r,N_b/2}) \sum_{m=0}^{M-1} \cos \left[r(\theta_m - \theta^{(r)} - \theta_0) \right] Q_m(A_p(\theta_m)) \quad (25)$$

where $\delta_{a,b}$ is the Kronecker delta and $\theta^{(r)}$ is such that

$$\sum_{m=0}^{M-1} \sin \left[r(\theta_m - \theta^{(r)} - \theta_0) \right] Q_m(A_p(\theta_m)) = 0 \quad (26)$$

We substitute (24) into the second summation of (23) and simplify:

$$\frac{1}{M} \sum_{r=0}^{M/2} N^{(r)} \sum_{m=0}^{M-1} \cos \left[r(\theta_m - \theta^{(r)} - \theta_0) \right] = N^{(0)} \quad (27)$$

We substitute (24) also in the term between square brackets in (23) that simplifies to:

$$\begin{aligned} & \sum_{m=0}^{M-1} e^{i2n(\theta_m - \theta_0)} Q_m(A_p(\theta_m)) = \\ & = \frac{1}{M} \sum_{r=0}^{M/2} N^{(r)} \sum_{m=0}^{M-1} e^{i2n(\theta_m - \theta_0)} \cos \left[r(\theta_m - \theta^{(r)} - \theta_0) \right] \\ & = \sum_{r=0}^{M/2} N^{(r)} e^{i2n\theta^{(r)}} \left\{ \frac{1}{M} \sum_{m=0}^{M-1} e^{i2n(\theta_m - \theta^{(r)} - \theta_0)} \cos \left[r(\theta_m - \theta^{(r)} - \theta_0) \right] \right\} \\ & = \frac{1}{2} N^{(2n)} e^{i2n\theta^{(2n)}} \end{aligned} \quad (28)$$

where it is assumed that the azimuthal order n is smaller or equal to $M/4$. Substituting (27) and (28) into (23) we obtain:

$$\frac{1}{2} \left\{ N^{(0)} - M\alpha + \frac{1}{2} N^{(2n)} e^{i2n\theta^{(2n)}} e^{2k\chi} \right\} \quad (29)$$

which is the second line of (7). We finally observe that for real-valued describing functions it holds that $\omega \approx \omega_0$, one obtains (7). We observe from the definition (25) that $N^{(0)}$ depends on $\{A, \chi, n\theta_0\}$ and that $N^{(2n)}$ depends on $\{A, \chi, 2n(\theta^{(n)} - \theta_0)\}$.